



## 22 **Abstract**

23 Cities in South and Southeast Asia are developing rapidly without routine, up-to-date  
24 knowledge of air pollutant precursor emissions. This data deficit can potentially be addressed  
25 for nitrogen oxides ( $\text{NO}_x$ ) by deriving city  $\text{NO}_x$  emissions from satellite observations of  
26 nitrogen dioxide ( $\text{NO}_2$ ) sampled under windy conditions.  $\text{NO}_2$  plumes of isolated cities are  
27 aligned along a consistent wind-rotated direction and a best-fit Gaussian is applied to estimate  
28 emissions. This approach currently relies on non-standardized selection of the area to sample  
29 around the city centre and Gaussian fits often fail or yield non-physical parameters. Here, we  
30 automate this approach by defining many (54) sampling areas that we test with Tropospheric  
31 Monitoring Instrument (TROPOMI)  $\text{NO}_2$  observations for 2019 over 19 cities in South and  
32 Southeast Asia. Our approach is efficient, adaptable to many cities, standardizes and eliminates  
33 sensitivity of the Gaussian fit to sampling area choice, and increases success of deriving annual  
34 emissions from 40-60% with one sampling area to 100% (all 19 cities) with 54. The annual  
35 emissions we estimate range from  $16 \pm 5 \text{ mol s}^{-1}$  for Yangon (Myanmar) and Bangalore (India)  
36 to  $125 \pm 41 \text{ mol s}^{-1}$  for Dhaka (Bangladesh). With the enhanced success of our approach, we  
37 find evidence from comparison of our top-down emissions to past studies and to inventory  
38 estimates that the wind rotation and EMG fit approach may be biased, as it does not adequately  
39 account for spatial and seasonal variability in  $\text{NO}_x$  photochemistry. Further methodological  
40 development is needed to enhance its accuracy and to exploit it to derive sub-annual emissions.

41

## 42 **Plain Language Summary**

43 Cities are a large source of nitrogen oxides ( $\text{NO}_x$ ) that go on to form many types of air pollutants  
44 of harm to human health. City  $\text{NO}_x$  emissions estimated with observations from space-based  
45 instruments are vital in regions that lack access to up-to-date, locally developed inventories.  
46 Success of obtaining satellite-derived emissions hinges on user selection of a sampling area  
47 around each city centre. Here we present an automated, efficient method that uses many (54)  
48 sampling areas. When tested on 19 cities in South and Southeast Asia, annual  $\text{NO}_x$  emissions  
49 are obtained for all 19 cities compared to about half the selected cities when using a single  
50 sampling area. With this updated approach, we estimate total  $\text{NO}_x$  emissions in 2019 that range  
51 from 23 kilotonnes for Yangon and Bangalore to almost 10-times more (181 kilotonnes) for  
52 Dhaka. The greater success of our updated approach also helps us identify that the accuracy of  
53 emissions derivation from satellite observations should be further improved by accounting for  
54 the influence of spatial and seasonal variability in  $\text{NO}_x$  photochemistry.

55

## 56 **1 Introduction**

57 Nitrogen oxides ( $\text{NO}_x \equiv \text{NO}_2 + \text{NO}$ ) react to form particulate nitrate and tropospheric  
58 ozone and deposit to sensitive habitats (Luo et al., 2019; Sillman, 1999), thus degrading air  
59 quality, altering climate, and adversely affecting human health and the environment (Grulke &  
60 Heath, 2020; Lelieveld et al., 2015; Yue et al., 2017; Marais et al., 2023). Controls targeting  
61 anthropogenic sources of  $\text{NO}_x$  have been extensively implemented in cities in Europe, the US  
62 and China (Curier et al., 2014; de Foy et al., 2016; Silvern et al., 2019). In cities in other parts  
63 of the world, particularly South and Southeast Asia,  $\text{NO}_x$  is increasing rapidly due to fast  
64 economic development and limited or absent air quality policies (Vohra et al., 2021; 2022).  
65 Vohra et al. (2022) used 14 years of satellite observations of  $\text{NO}_2$  from the Ozone Monitoring  
66 Instrument (OMI) to infer increases of  $\sim 1\text{-}14 \text{ \% a}^{-1}$  in surface  $\text{NO}_2$  pollution in almost all rapidly  
67 developing large cities in South and Southeast Asia. Only in Jakarta did  $\text{NO}_2$  decline due to  
68 emission controls applied to vehicles (Vohra et al., 2022). Population projections suggest that,

69 by 2100, one-fifth of the world's most populous cities will be in Southeast Asia (Hoornweg &  
70 Pope, 2017), necessitating reliable and up-to-date NO<sub>x</sub> emissions estimates for assessing the  
71 impact of this growth on urban air quality and for informing air quality policies.

72 Bottom-up inventories provide estimates of anthropogenic NO<sub>x</sub> emissions, but publicly  
73 available versions for South and Southeast Asia do not adequately represent contemporary  
74 local conditions, as these are derived using outdated activity data, are resource-intensive to  
75 produce so lag the present day, are at spatial resolutions that are coarser than many cities in the  
76 region, and data needed to compile the inventories do not exist for many countries (Kurokawa  
77 & Ohara, 2020). The two most used bottom-up inventories for these regions are the Regional  
78 Emission inventory in Asia (REAS) (Kurokawa & Ohara, 2020) and the inventory known as  
79 MIX, a mosaic of REAS and other regional inventories (Li et al., 2017). REAS and MIX are  
80 at ~25 km resolution, MIX only covers 2 years of data, and the most recent years are 2015 for  
81 REAS and 2010 for MIX. Still, REAS and inventories used to create MIX are routinely  
82 incorporated in global inventories such as the Community Emissions Data System (CEDS<sub>GBD-</sub>  
83 <sub>MAPS</sub>) (McDuffie et al., 2020), and Hemispheric Transport of Air Pollution (HTAP) (Crippa et  
84 al., 2023).

85 Independent and contemporary estimates of city NO<sub>x</sub> emissions can be derived with  
86 satellite observations of tropospheric NO<sub>2</sub> vertical column densities (VCDs) without the need  
87 for resource-intensive computer models. A method first proposed by Beirle et al. (2011)  
88 involves selecting isolated cities and treating these as large point sources of NO<sub>x</sub>. In this  
89 approach, individual satellite pixels within a target domain centred on a city centre were split  
90 into eight major wind directions to resolve the city plume in each direction. A mathematical  
91 function was then fit to the plume to account for its Gaussian shape and exponential decay of  
92 NO<sub>2</sub>. This fit, referred to as an Exponential Modified Gaussian (EMG), yields parameters that  
93 are then used to estimate NO<sub>x</sub> emissions. It also yields an effective lifetime of NO<sub>x</sub> for the city  
94 plume that is dominated by dispersion for the windy conditions sampled. As dispersion  
95 dominates, the derived lifetime is much shorter than the chemical lifetime of NO<sub>x</sub> that includes  
96 conversion to nitric acid (HNO<sub>3</sub>) or organic nitrates (de Foy et al., 2014; Laughner & Cohen,  
97 2019) and, to a lesser extent, dry deposition of NO<sub>2</sub> (Zhang et al., 2012). Beirle et al. (2011)  
98 used OMI observations of NO<sub>2</sub> to derive NO<sub>x</sub> emissions for eight global megacities. The Beirle  
99 et al. (2011) approach required many (four) years of OMI data to achieve distinct plumes in  
100 each wind direction.

101 Valin et al. (2013) expanded on the approach developed by Beirle et al. (2011) by  
102 demonstrating that all satellite data can instead be aligned along a single upwind-downwind  
103 direction relative to the city centre. This approach reduced the number of observations needed  
104 to distribute the data by wind direction and so extended application to a greater number of  
105 geographically isolated cities over shorter sampling periods. Wind rotation of OMI  
106 observations and the EMG fit have since been used to calculate city NO<sub>x</sub> emissions  
107 predominantly in the US (de Foy et al., 2014; Goldberg et al., 2019a; Lu et al., 2015) and for  
108 select cities worldwide (Goldberg et al., 2021). Following the 2017 launch of the higher spatial  
109 resolution TROPOspheric Monitoring Instrument (TROPOMI), the wind rotation, EMG fit,  
110 and related approaches have been extended to smaller isolated cities and shorter sampling  
111 periods than was possible with OMI. Applications include cities in western Europe (Lorente et  
112 al., 2019; Pope et al., 2022), China (Wu et al., 2021), the US (Goldberg et al., 2019b), and  
113 worldwide (Lange et al., 2022), as well as investigating changes in NO<sub>x</sub> emissions due to  
114 COVID-19 lockdown measures in the New York Metropolitan Area (Tzortziou et al., 2022)  
115 and for select cities in India, Argentina, and Spain (Lange et al., 2022). So far, the wind rotation  
116 and EMG fit has only been applied to 5-13 cities in South and Southeast Asia as part of global  
117 studies (Goldberg et al., 2021; Lange et al., 2022).

118 Even though there has been substantial development and use of the EMG fit, it still  
119 requires that a user define a sampling area around the city that effectively captures the wind  
120 rotated plume. The area selected varies with city size and plume length (Lu et al., 2015;  
121 Goldberg et al., 2019a; Lange et al., 2022). This approach often yields no or poor EMG fits  
122 and non-physical best-fit parameters (Laughner & Cohen, 2019), decreasing the likelihood of  
123 deriving top-down emissions. Selecting appropriate city-specific areas for the wide-ranging  
124 city sizes in South and Southeast Asia is also time consuming and not standardized.

125 Here we develop a near-automated and efficient EMG fitting routine for deriving  
126 annual city NO<sub>x</sub> emissions, demonstrate the utility of this automation by applying it to  
127 TROPOMI NO<sub>2</sub> observations over isolated cities in South and Southeast Asia with wide-  
128 ranging city sizes, compare our top-down emissions to past studies and a global bottom-up  
129 inventory, and exploit the greater success of our updated sampling to identify opportunities to  
130 further develop the EMG fit approach.

131

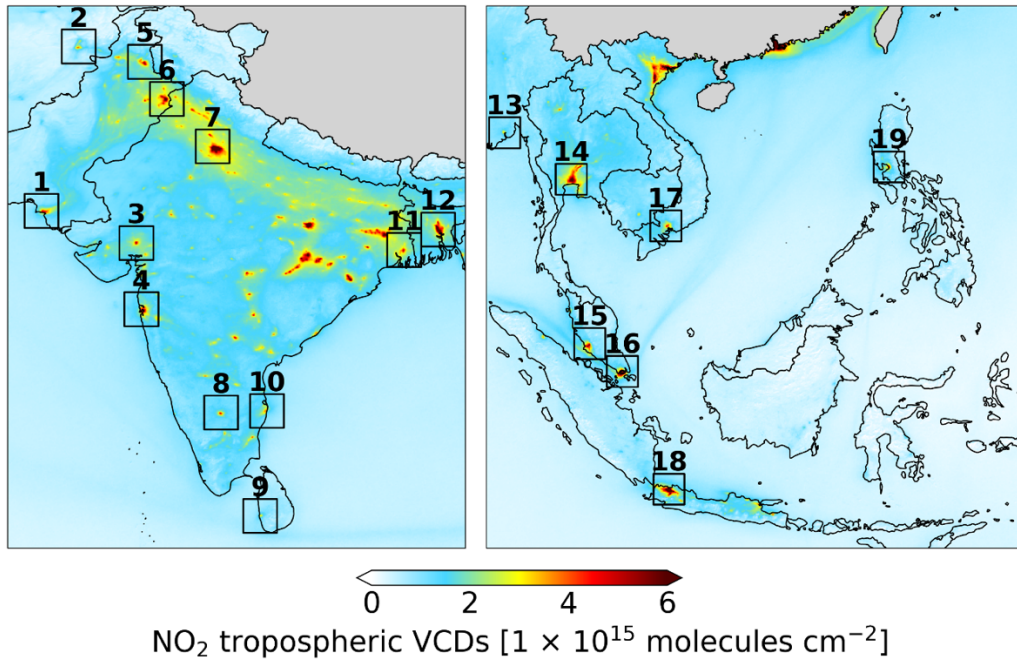
## 132 **2 Materials and Methods**

### 133 **2.1 TROPOMI NO<sub>2</sub> and City Selection**

134 We use Level 2 TROPOMI NO<sub>2</sub> tropospheric column VCDs for 2019 from the  
135 Sentinel-5P Products Algorithm Laboratory (S5P-PAL) portal ([https://data-portal.s5p-  
136 pal.com/](https://data-portal.s5p-pal.com/); last acquired 30 January 2022). These data have been retrieved with a consistent  
137 algorithm (version 02.03.01) and corrected for a low bias in NO<sub>2</sub> over polluted scenes (Eskes  
138 et al., 2021). TROPOMI achieves daily global coverage with a swath width of 2600 km, an  
139 equator crossing time of 13:30 local solar time (LST), and a nadir pixel resolution that increased  
140 on 5 August 2019 from 7 km × 3.5 km to 5.5 km × 3.5 km. We use cloud-free, high-quality  
141 data identified with a quality flag ≥ 0.75 (van Geffen et al., 2021).

142 To identify isolated cities appropriate for top-down estimate of NO<sub>x</sub> emissions, we first  
143 oversample TROPOMI NO<sub>2</sub> to obtain high-resolution gridded annual means (0.05° × 0.05°;  
144 ~6 km latitude × ~5 km longitude) by weighting areas of overlap between the satellite pixels  
145 and cells on a fixed latitude-longitude grid using tessellation (Sun et al., 2018). We use the  
146 resultant gridded TROPOMI NO<sub>2</sub> shown in Figure 1 to manually select 19 cities that are  
147 isolated hotspots. The 19 selected cities are Karachi, Islamabad, and Lahore in Pakistan; Kabul  
148 in Afghanistan; Ahmedabad, Mumbai, Delhi, Bangalore, Chennai, and Kolkata in India;  
149 Colombo in Sri Lanka; Dhaka in Bangladesh; Yangon in Myanmar; Bangkok in Thailand;  
150 Kuala Lumpur in Malaysia; the sovereign city Singapore; Ho Chi Minh City in Vietnam;  
151 Jakarta in Indonesia; and Manila in the Philippines. Other hotspots in Figure 1 are either not  
152 cities, such as the coal-fired power plants concentrated in eastern India, or are not isolated, such  
153 as Hanoi, Haiphong and Nam Dinh in northern Vietnam.

154



155

156 **Figure 1.** Annual mean TROPOMI tropospheric NO<sub>2</sub> VCDs over South and Southeast Asia in  
 157 2019. Maps show South (left) and Southeast (right) Asia TROPOMI NO<sub>2</sub> oversampled to 0.05°  
 158 × 0.05°. The 19 selected cities, numbered from east to west, are Karachi (1), Islamabad (5),  
 159 and Lahore (6) in Pakistan; Kabul (2) in Afghanistan; Ahmedabad (3), Mumbai (4), Delhi (7),  
 160 Bangalore (8), Chennai (10), and Kolkata (11) in India; Colombo (9) in Sri Lanka; Dhaka (12)  
 161 in Bangladesh; Yangon (13) in Myanmar; Bangkok (14) in Thailand; Kuala Lumpur (15) in  
 162 Malaysia; the sovereign city Singapore (16); Ho Chi Minh City (17) in Vietnam; Jakarta (18)  
 163 in Indonesia; and Manila in the Philippines (19).

164

## 165 2.2 Wind Rotation and EMG Fit

166 Figure 2 illustrates the major steps involved in the wind rotation and EMG fit to derive  
 167 annual NO<sub>x</sub> emissions for Singapore. The wind fields we use to calculate wind direction and  
 168 speed to retain TROPOMI NO<sub>2</sub> observations under windy conditions are the fifth generation  
 169 European ReAnalysis (ERA5) 3D hourly *u* and *v* wind components  
 170 (<https://cds.climate.copernicus.eu/cdsapp#!/home>; last acquired 18 March 2022) provided at  
 171 0.25° × 0.25° resolution. At each TROPOMI NO<sub>2</sub> pixel, we compute collocated mean ERA5  
 172 wind speeds and directions 30 min around 13:30 LST, the TROPOMI overpass time, in the  
 173 lowest 5 layers (≥ 900 hPa) to capture dispersion of mixed-layer near-surface NO<sub>2</sub> plumes.  
 174 Within a 4° × 4° domain around each city centre, we isolate TROPOMI pixels with coincident  
 175 wind speeds > 2 m s<sup>-1</sup>, the threshold typically used for windy conditions (Beirle et al., 2011;  
 176 Pope et al., 2022). We rotate each TROPOMI NO<sub>2</sub> pixel by the angle of its wind direction,  
 177 preserving the distance of the pixel from the city centre. This aligns all pixels along the same  
 178 “upwind-downwind” direction that in our work is from north to south (Figure 2(a)). After wind  
 179 rotating all pixels in a year (as in Figure 2), we grid pixels onto a uniform 0.05° × 0.05° grid  
 180 using simple point-in-box averaging (Figure 2(a)) and fill empty grid cells (grey squares in  
 181 Figure 2(a)) using nearest-neighbour interpolation to reduce low biases in the steps that follow.

182 Next, the 2D map in Figure 2(b) is converted to 1D line densities by summing all grid  
 183 cells in the across-wind (east-to-west) direction in 0.05° upwind-downwind (north-to-south)  
 184 increments. In the standard approach, a single area smaller than the 4° × 4° domain is used,

185 defined by the distance upwind, downwind, and across-wind of the city centre. Instead of using  
 186 a single area, we define multiple areas that encompass the range of sizes typically used in past  
 187 studies (Goldberg et al., 2021; Lange et al., 2022; Laughner & Cohen, 2019). These, defined  
 188 as distances from the city centre, are 0.5°, 0.75°, and 1° upwind, 0.5°, 0.75°, 1.0°, 1.25°, 1.5°,  
 189 1.75°, 2.0° downwind, and 0.5°, 0.75°, and 1.0° across-wind, with the requirement that the  
 190 distance downwind of the city centre is  $\geq$  the distance upwind to capture the extent of the city  
 191 plume. This yields 54 areas and associated line densities. The sizes of the smallest and largest  
 192 areas sampled and the across-wind 0.05° increments summed to obtain line densities in the  
 193 smallest area sampled are shown in Figure 2(b).

194 The EMG model we use to fit to the observed 1D line densities is the Laughner &  
 195 Cohen (2019) formulation:

$$196 \quad F(x|a, x_0, \mu_x, \sigma_x, B) = \frac{a}{2x_0} \exp\left(\frac{\mu_x}{x_0} + \frac{\sigma_x^2}{2x_0^2} - \frac{x}{x_0}\right) \operatorname{erfc}\left(-\frac{1}{\sqrt{2}}\left[\frac{x-\mu_x}{\sigma_x} - \frac{\sigma_x}{x_0}\right]\right) + B \quad (1),$$

197 where  $x$  is the distance of each line density upwind and downwind of the city centre (Figure  
 198 2(c)) and  $a$ ,  $x_0$ ,  $\mu_x$ ,  $\sigma_x$  and  $B$  are best-fit parameters. Of these,  $a$  is total NO<sub>2</sub> in the plume (in  
 199 moles),  $x_0$  is the  $e$ -folding distance or length scale of NO<sub>2</sub> decay (in km),  $\mu_x$  is the location of  
 200 the apparent source relative to the city centre (in km) or the peak of the Gaussian fit that in  
 201 Figure 2(c) is located  $\sim 20$  km downwind or south of the city centre,  $\sigma_x$  is the Gaussian  
 202 smoothing length scale (in km) that is  $\sim 2.355 \times$  the Full Width at Half Maximum (FWHM),  
 203 and  $B$  is background NO<sub>2</sub> (in moles m<sup>-1</sup>).

204 We use initial guesses for the best-fit parameters in Equation (1) that are similar to those  
 205 from Laughner & Cohen (2019), but our fitting procedure differs. Laughner & Cohen (2019)  
 206 used a non-linear interior point minimization algorithm (the *fmincon* function in MATLAB) to  
 207 optimize model parameters with 10 iterations per line density. Instead, we perform the fit with  
 208 the *scipy.optimize.curve\_fit* module from SciPy Python package version 1.7.3 and iterate on  
 209 the fit until the difference in fitting parameters between the current and previous iteration is  
 210 negligible ( $< 0.001\%$ ) for at most 10 iterations. Fit convergence is usually achieved after 3  
 211 iterations. Only good-quality fits are retained, identified with goodness-of-fits ( $R^2$ )  $> 0.8$ , as in  
 212 Laughner & Cohen (2019). We further screen for physically implausible best-fit parameters  
 213 using criteria similar to Laughner & Cohen (2019):  $a$  is positive,  $x_0$  is at least 1.6 km  
 214 (approximately  $1/e$  of the grid resolution),  $\mu_x$  is within the sampling area, the emission width  
 215 is less than the  $e$ -folding distance ( $\sigma_x < x_0$ ), background NO<sub>2</sub> is positive and less than the  
 216 maximum line density value, and the  $e$ -folding distance occurs between the plume centre and  
 217 the edge of the sampling area. We introduce an additional requirement to ensure that  $x_0$  is within  
 218 the sampling area ( $x_0 < \text{length of sampling area downwind of the city centre}$ ).

219 The Singapore example in Figure 2 is an ideal city, as all 54 EMG fits are successful.  
 220 Figure 2(c) shows that the observed line densities are most sensitive to the across-wind length,  
 221 as this determines the amount of NO<sub>2</sub> summed to yield each line density. We will demonstrate  
 222 in Section 3 that for many of the cities in Figure 1 a large number of EMG fits fail to meet the  
 223 conditions for success, necessitating as many as 54 fits.

224 The successful EMG fits are used to calculate effective NO<sub>x</sub> lifetimes ( $\tau_{NO_x}$ ; reported  
 225 in h) and midday NO<sub>x</sub> emissions ( $E_{NO_x}$ ; in moles s<sup>-1</sup>):

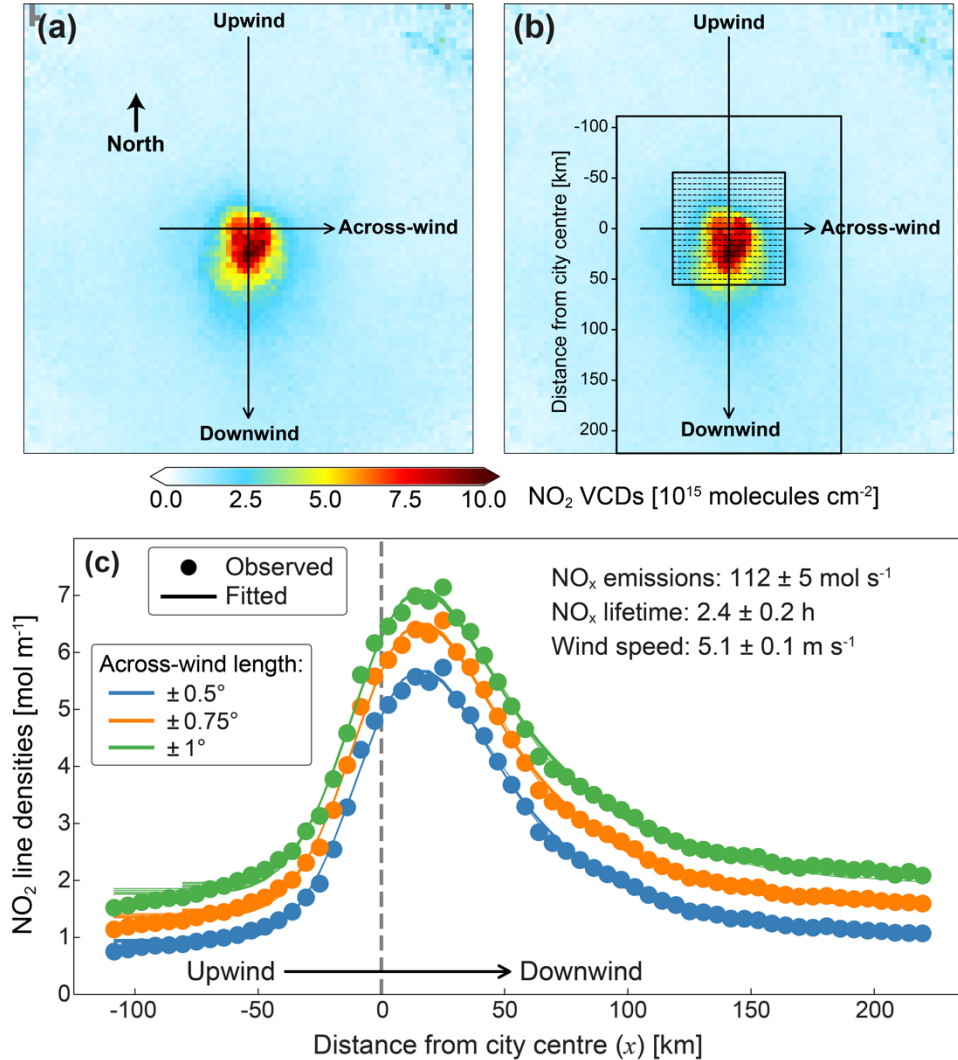
$$226 \quad \tau_{NO_x} = \frac{x_0}{\omega} \quad (2)$$

$$227 \quad E_{NO_x} = \gamma \times \frac{a}{\tau_{NO_x}} \quad (3),$$

228 where  $\omega$  is the sampling area mean wind speed (in  $\text{m s}^{-1}$ ) and  $\gamma$  is the unitless molar ratio of  
 229  $[\text{NO}_x]/[\text{NO}_2]$  to convert moles  $\text{NO}_2$  to moles  $\text{NO}_x$ . The up to 54 individual estimates of  $\tau_{\text{NO}_x}$   
 230 and  $E_{\text{NO}_x}$  are averaged to obtain values for each city.

231

232



233

234 **Figure 2.** Illustration of major steps in the wind rotation and EMG fit to derive annual  $\text{NO}_x$   
 235 emissions for Singapore. The main steps in each panel are wind rotate and grid windy scene  
 236 TROPOMI  $\text{NO}_2$  pixels to  $0.05^\circ \times 0.05^\circ$  (a), fill data gaps (b), and fit the EMG function (Eq.  
 237 (1)) (solid lines) to observed line densities (filled circles) (c). In (b), black rectangles show the  
 238 extent of the largest and smallest sampling areas and dashed lines in the smallest area show the  
 239  $0.05^\circ$  increments used to calculate the line densities in (c). All 54 successful EMG fits, 18 lines  
 240 for each of the three across-wind lengths, are shown in (c). Values in (c) give the mean and  
 241 standard deviation of the city  $\text{NO}_x$  emissions (Eq. (3)), effective  $\text{NO}_x$  lifetime (Eq. (2)), and  
 242 sampling area ERA5 wind speed. The goodness-of-fit ( $R^2$ ) is  $\geq 0.99$  for all fits in (c).

243

244 We use the same  $[\text{NO}_x]/[\text{NO}_2] = 1.32$  value as Beirle et al. (2011) and subsequent  
 245 studies to represent rapid cycling between  $\text{NO}$  and  $\text{NO}_2$ . Liu et al. (2022) determined with  
 246 synthetic experiments that city  $\text{NO}_x$  emissions are relatively unaffected by variability in  
 247  $[\text{NO}_x]/[\text{NO}_2]$ , but that study was for US cities. Surface measurements aid in determining

248 suitability of  $[\text{NO}_x]/[\text{NO}_2] = 1.32$ , but these are limited to cities in India and have data quality  
249 issues (Vohra et al., 2021). Instead, we use the GEOS-Chem model to assess suitability of the  
250 1.32 value. We simulate the model in 2019 and sample the lowest model layer around the  
251 TROPOMI overpass time. We use output from a coarse and finer resolution version of GEOS-  
252 Chem to also test sensitivity of this ratio to model resolution, especially given many of these  
253 cities are coastal (Figure 1). We use the classical configuration of the model that operates on a  
254 single computational node, called GEOS-Chem Classic (GCCClassic), and the high-  
255 performance model configuration (GCHP) that is a parallelized across multiple computational  
256 nodes to enable finer resolution global simulations (Eastham et al., 2018). GCCClassic is version  
257 13.3.4 (<https://doi.org/10.5281/zenodo.5764874>) run on a fixed  $2^\circ \times 2.5^\circ$  global grid and  
258 GCHP is version 13.4.1 (<https://doi.org/10.5281/zenodo.6564711>) run on a C360 global grid  
259 ( $\sim 25 \text{ km} \times \sim 31 \text{ km}$ ). GCCClassic and GCHP use the same vertical grid and chemical mechanism.  
260 For GCCClassic, grid squares that overlap with each city are sampled, whereas for GCHP, we  
261 use city sampling extents determined from a combination of administrative and geographic  
262 boundary shapefiles and Google Maps (Figure S1). Midday sampling is at 12:00 to 15:00 LST  
263 from GCCClassic and 13:00 to 14:00 LST from GCHP. At midday,  $\text{NO}_x$  is in photochemical  
264 steady state, so the relative abundance of NO and  $\text{NO}_2$  is insensitive to the extent of the  
265 sampling window around midday (Potts et al., 2021).

266 We calculate uncertainties in the  $\text{NO}_x$  emissions by adding individual errors in  
267 quadrature. These include best-fit parameters  $x_0$  and  $a$ , sampling area mean wind speed  $\omega$ , the  
268 TROPOMI  $\text{NO}_2$  observations, and  $[\text{NO}_x]/[\text{NO}_2]$ . We use the relative standard deviation from  
269 all successful EMG fits to calculate city-specific errors in  $x_0$  and  $a$ . For  $\omega$ , we consider errors  
270 due to the choice of spatial and temporal sampling and the threshold used for windy conditions.  
271 We use the Beirle et al. (2011) estimated 10% error in temporal sampling choice and 5% error  
272 due to vertical sampling choice. We conduct our own tests of the sensitivity to threshold and  
273 spatial sampling choice. For  $[\text{NO}_x]/[\text{NO}_2]$  we assess whether the 10% error attributed to this  
274 variable by Beirle et al. (2011) is appropriate by quantifying the percent deviation of GCCClassic  
275 and GCHP  $[\text{NO}_x]/[\text{NO}_2]$  from 1.32. Beirle et al. (2011) applied a 30% error to OMI that is also  
276 appropriate for TROPOMI. Even though uncertainties in TROPOMI slant columns ( $\text{NO}_2$  along  
277 the viewing path) are much less than those from OMI (van Geffen et al., 2020), the air mass  
278 factor used to convert slant columns to VCDs remains the largest contributor to errors in  $\text{NO}_2$   
279 VCDs and is similar for OMI and TROPOMI (van Geffen et al., 2021).

## 280 **2.3 Bottom-up Anthropogenic Emissions**

281 We compare our top-down estimates to anthropogenic  $\text{NO}_x$  emissions from the widely  
282 used bottom-up HTAP inventory version 3 (HTAP\_v3) (Crippa et al., 2023). HTAP\_v3 has  
283 high enough spatial resolution ( $0.1^\circ \times 0.1^\circ$ ) to resolve cities selected in Figure 1. The most  
284 recent year is 2018, achieved by extending emissions from the regional REAS inventory ending  
285 in 2015 to the year 2018 with trends from the Emissions Database for Global Atmospheric  
286 Research (EDGAR) inventory. The same sampling boundaries as GCHP are used (Section 2.2;  
287 Figure S1). The HTAP\_v3  $\text{NO}_x$  emissions include contributions from aviation, transport (road,  
288 rail, pipeline, inland waters), shipping, energy, industry, and residential sectors.

289 Cities targeted can be influenced by non-anthropogenic  $\text{NO}_x$  sources, such as open  
290 burning of biomass (Marvin et al., 2021) and natural sources such as soils (Weng et al., 2020)  
291 and lightning (Miyazaki et al., 2014). We assess suitability of comparing our top-down  
292 emissions to anthropogenic bottom-up emissions only by determining the percent contribution  
293 of anthropogenic emissions to total  $\text{NO}_x$  emissions. To do this, we simulate total  $\text{NO}_x$  emissions  
294 with the Harmonized Emissions Component (HEMCO) standalone model version 3.0.0  
295 (<https://zenodo.org/records/4984639>; last accessed 20 March 2022) (Lin et al., 2021) and

296 sample the same spatial extent as GCHP and HTAP\_v3 (Figure S1). HEMCO is run at a spatial  
297 resolution of  $0.25^\circ \times 0.3125^\circ$  ( $\sim 28$  km latitude  $\times \sim 33$  km longitude). HEMCO calculates open  
298 biomass burning emissions using the Global Fire Emissions Database with small fires  
299 (GFED4s) inventory (Randerson et al., 2017) and reads in and processes lightning and soil  $\text{NO}_x$   
300 from offline emissions at the same resolution as HEMCO (Murray et al., 2012; Weng et al.,  
301 2020).

302 Bottom-up emissions from HTAP\_v3 are 24-h means, whereas top-down estimates  
303 derived using TROPOMI are representative of midday emissions. Goldberg et al. (2021)  
304 multiplied satellite-derived midday  $\text{NO}_x$  emissions by 0.77 to convert midday top-down  $\text{NO}_x$   
305 emissions to 24-h means for comparison to bottom-up inventories. This value was inferred  
306 from bottom-up emissions estimates for the Netherlands, so may not be suitable for the selected  
307 cities in South and Southeast Asia. The hourly scaling factors used by HEMCO for the chosen  
308 cities range from 0.70 to 1.16. These are for the year 2000 and are extrapolations of values for  
309 conditions in Europe, so may not be suitable for the year and cities targeted in this study. Given  
310 this, we do not scale top-down emissions and instead discuss whether differences in averaging  
311 times contribute to discrepancies between top-down and bottom-up emissions estimates.

312

### 313 **3 Results and Discussion**

#### 314 **3.1 Wind Rotation and EMG Fit Metrics**

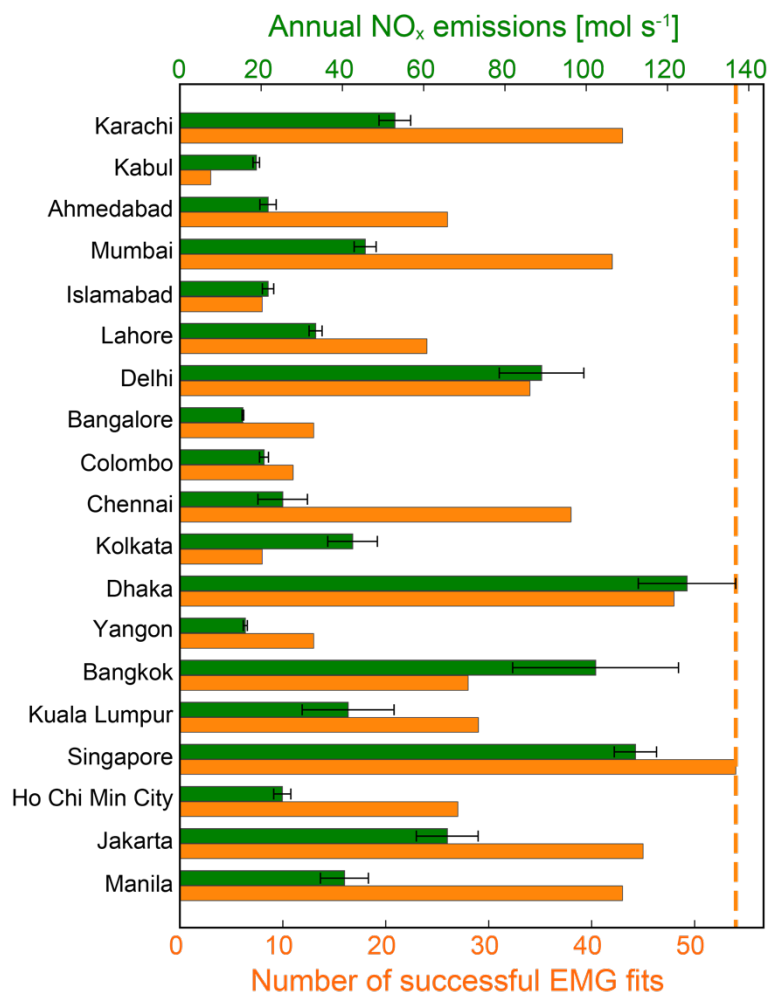
315 Isolating windy condition ( $> 2 \text{ m s}^{-1}$ ) satellite pixels removes 8-34% of all 2019 quality-  
316 and cloud-screened TROPOMI  $\text{NO}_2$  pixels for most cities in Figure 1. Cities with greater data  
317 loss are Lahore (43% data loss), Kabul (58%) and Islamabad (63%). No spatial data gap filling  
318 (Section 2.2, Figure 2) is needed within the areas sampled, due to the high sampling frequency  
319 of TROPOMI. If only a single domain size is selected, annual EMG fits meet all criteria for  
320 success for 7 to 12 of the 19 cities in Figure 1, depending on the sampling area chosen. Using  
321 our extended method, we successfully derive annual  $\text{NO}_x$  emissions for all 19 cities, due to the  
322 enhanced probability of obtaining at least one successful EMG fit.

323 Figure shows the number of successful EMG fits (orange bars) range from 3 (Kabul) to  
324 all 54 (Singapore). Singapore, Dhaka, Jakarta, Karachi, Manila, and Mumbai are least impacted  
325 by the choice of sampling area. The 6 cities in Figure 3 with  $< 20$  fits are most likely to fail if  
326 only a single sampling area is used. For all retained EMG fits, differences between observed  
327 and fitted  $\text{NO}_2$  line densities, the fit residuals, are negligible. The most common causes for a  
328 failed EMG fit rank as: background  $\text{NO}_2$  ( $B$  in Equation (1))  $>$  maximum  $\text{NO}_2$  line density (36%  
329 of all fits conducted),  $R^2 \leq 0.8$  (24%), emission width  $>$   $e$ -folding distance (19%), total plume  
330  $\text{NO}_2$  ( $a$  in Equation (1))  $<$  0 (13%), and  $e$ -folding distance  $>$  the downwind length of the  
331 sampling area (12%). Multiple causes can co-occur in a single fit, so cumulative percentages  
332 exceed 100%.

333 We also test sensitivity of top-down  $\text{NO}_x$  emissions to the choice of wind speed  
334 threshold and horizontal sampling extent to attribute an error to these. For this, we apply a  
335 stricter wind speed threshold of  $3 \text{ m s}^{-1}$  and test the difference in  $\text{NO}_x$  emissions if instead of  
336 filtering for windy conditions using pixel-mean wind fields, we calculate a sampling-area mean  
337 wind speed to filter for windy conditions as in Goldberg et al. (2019a). We apply these  
338 conditions to a mid-sized sampling area of  $0.75^\circ$  upwind,  $1.5^\circ$  downwind, and  $\pm 0.75^\circ$  across-  
339 wind. Variability in  $\text{NO}_x$  emissions for cities with successful EMG fits for all 4 wind sampling  
340 conditions is at most 10% (Figure S2). Given these results, we attribute a 10% error to the  
341 choice of horizontal sampling and to the wind speed threshold.

342 GClassic (coarse resolution) annual mean  $[\text{NO}_x]/[\text{NO}_2]$  for the target cities ranges  
 343 from 1.25 (Dhaka) to 1.41 (Kabul). The range in ratios from GCHP (finer resolution) is wider  
 344 at 1.24 (Ahmedabad) to 1.64 (Kolkata). The difference in ratios between the coarse and fine  
 345 resolution models is typically  $\pm 10\%$ , except for a few cities with ratios from the fine resolution  
 346 model that exceed the coarse resolution model by 14% for Singapore, 16% for Lahore, 23%  
 347 for Dhaka, and 23% for Kolkata. This is because the fine resolution model better resolves the  
 348 city plume that includes a greater proportion of  $\text{NO}_x$  as  $\text{NO}$  from fresh emission sources. As  
 349 the difference between the model city ratios and the 1.32 value is  $\pm 10\%$  for most cities, we use  
 350 the same 10% error for  $[\text{NO}_x]/[\text{NO}_2]$  as Beirle et al. (2011).

351



352  
 353 **Figure 3.** Successful EMG fits and top-down  $\text{NO}_x$  emissions for the cities targeted in this study.  
 354 Bars are emissions (green) and the corresponding number of successful fits (orange). Black  
 355 error lines are  $\text{NO}_x$  emission standard deviations for all successful fits. The orange dashed line  
 356 at 54 indicates the maximum possible EMG fits. Emissions multiplied by  $\sim 1.45$  yields  
 357 emissions in  $\text{Gg NO}_2 \text{ a}^{-1}$ .

358

### 359 3.2 Top-Down $\text{NO}_x$ Emissions

360 Green bars in Figure 3 show the mean annual top-down  $\text{NO}_x$  emissions for all cities  
 361 (values are in Table S1). These range from  $\sim 16 \text{ mol s}^{-1}$  for Bangalore and Yangon to  $\sim 125 \text{ mol}$   
 362  $\text{s}^{-1}$  for Dhaka. The range in the total mass of  $\text{NO}_x$  emitted for these cities, assuming the midday

363 emission rate is reasonably representative of the 24-h emission rate, is 23-181 Gg NO<sub>x</sub> as NO<sub>2</sub>.  
364 Emissions for most cities are < 50 mol s<sup>-1</sup> (<73 Gg NO<sub>x</sub> as NO<sub>2</sub> a<sup>-1</sup>). Cities with emissions  
365 between 50-100 mol s<sup>-1</sup> (73-145 Gg NO<sub>x</sub> as NO<sub>2</sub> a<sup>-1</sup>) include Karachi, Delhi, and Jakarta and >  
366 100 mol s<sup>-1</sup> (> 145 Gg NO<sub>x</sub> as NO<sub>2</sub> a<sup>-1</sup>) include Bangkok, Singapore, and Dhaka. Emission  
367 rates for Bangkok, Dhaka and Singapore are comparable to the range of top-down emissions  
368 estimated for large, polluted cities in China using the EMG approach (Wu et al., 2021). The  
369 effective lifetimes for the cities in Figure 1 (shown in Figure S3) range from 1.2 h for Colombo  
370 to 6.3 h for Kuala Lumpur. Variability in effective lifetimes depends most strongly on the  
371 downwind extent of the plume. The Pearson's correlation coefficient, R, between city mean  
372 effective lifetimes and x<sub>0</sub> values is 0.90.

373 For the target cities, the relative standard deviations of annual NO<sub>x</sub> emissions (black  
374 error lines in Figure 3) range from just 1% for Bangalore to 27% for Kuala Lumpur. This is far  
375 less than the equivalent Gaussian fit uncertainty of 10-50% estimated by Beirle et al. (2011)  
376 for a single sampling area. The relatively large variability in Kuala Lumpur NO<sub>x</sub> emissions is  
377 because the smaller EMG sampling areas do not fully encompass the elongated wind rotated  
378 city NO<sub>2</sub> plume, causing a low bias in NO<sub>x</sub> emissions for the smaller areas sampled. The effect  
379 of this is dampened by the almost 30 successful fits used to obtain mean NO<sub>x</sub> emissions for this  
380 city. The relative standard deviations of the NO<sub>x</sub> lifetimes (Figure S3) range from 3% for  
381 Bangalore to 37% for Chennai. The relative standard deviations of other parameters are ~6%  
382 for wind speeds (Figure S4), 4% (Bangalore) to 38% (Chennai) for x<sub>0</sub>, and 4% (Kabul and  
383 Bangalore) to 37% (Bangkok) for *a*.

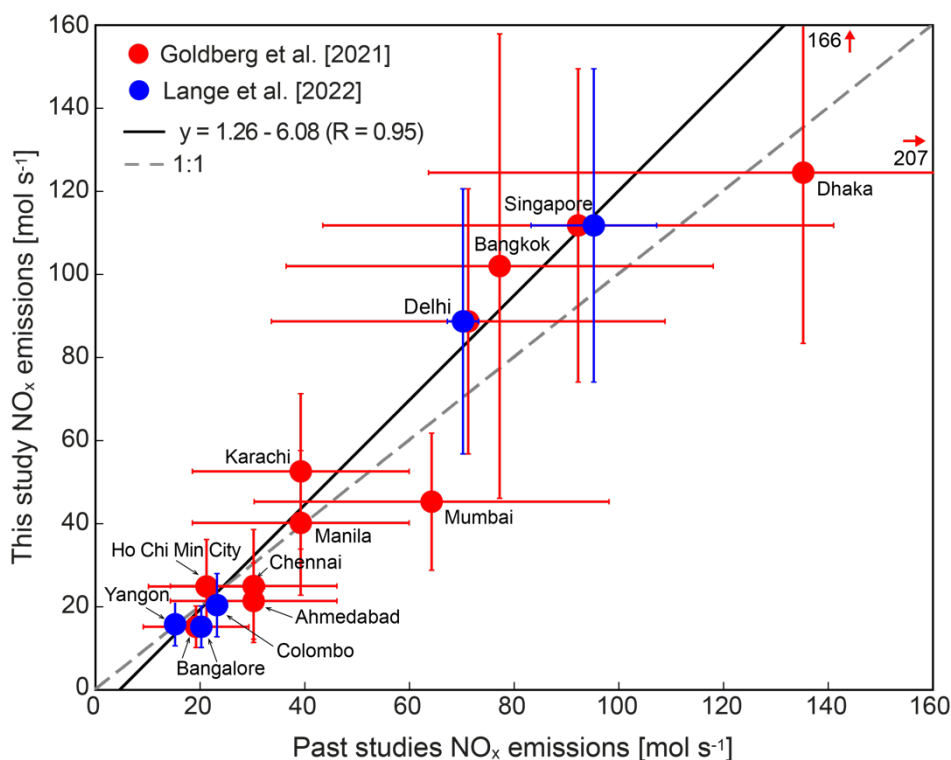
384 The overall uncertainty in annual NO<sub>x</sub> emissions we obtain by adding all error  
385 contributions in quadrature ranges from 32% for Bangalore and Yangon to 55% for Bangkok.  
386 Values for all cities are in Table S1. The TROPOMI NO<sub>2</sub> VCDs make the largest contribution  
387 to the overall uncertainty. The higher-end of our uncertainty estimates is similar to the typical  
388 ~50% uncertainty reported in past studies (Beirle et al., 2011; Verstraeten et al., 2018; Goldberg  
389 et al., 2021). We use our overall uncertainties in the comparison of our top-down emissions to  
390 values from the literature and from HTAP in the sections that follows.

391

### 392 **3.3 Comparison to Top-Down Estimates from Past Studies**

393 To assess our approach, we compare in Figure 4 our annual NO<sub>x</sub> emissions to values  
394 from past studies that used similar sampling time periods and a single sampling area. These  
395 include multiyear (2017-2019) mean emissions from Goldberg et al. (2021) obtained using the  
396 OMI sensor and emissions from Lange et al. (2022) obtained with select days of TROPOMI  
397 data from 2018 to 2020. Goldberg et al. (2021) estimated emissions for 10 of the 19 cities in  
398 our study. These we read from their Figure S10 for Karachi, Figure S11 for 4 cities in India,  
399 and Figure S13 for 5 cities in Southeast Asia and divide by the 0.77 midday to 24-h scaling  
400 factor used in that study. Emissions are reported by Lange et al. (2022) for 5 of the 19 cities in  
401 our study. Based on the regression statistics in Figure 4, our emissions are typically ~26% more  
402 than estimates from these past studies. Exceptions are Mumbai, Ahmedabad, and Chennai that  
403 in our study are 16-29% less than Goldberg et al. (2021). Lange et al. (2022) used an earlier  
404 version of the TROPOMI data product that has a known low bias in NO<sub>2</sub> VCDs over very  
405 polluted scenes (van Geffen et al., 2022). Differences in TROPOMI data products are the likely  
406 cause for our higher Delhi (by 27%) and Singapore (by 18%) emissions. Relatively small error  
407 estimates from Lange et al. (2022) are because they only propagate error contributions from  
408 the wind speed data and the EMG fit.

409



410

411 **Figure 4.** Comparison of our and past top-down NO<sub>x</sub> emissions. Symbols compare our  
 412 emissions to those from Goldberg et al. (2021) (red) and Lange et al. (2022) (blue). Error bars  
 413 are overall uncertainties for our study (Section 2.2, Table S1), the same 53% uncertainty  
 414 applied to all cities by Goldberg et al. (2021) and the city-specific uncertainties for Lange et al.  
 415 (2022). Lines are the Theil regression fit (solid black) and 1:1 relationship (dashed grey). Inset  
 416 text gives the regression statistics and Pearson’s correlation coefficient (R). Arrows and inset  
 417 text for Dhaka give the error values that extend beyond the plotting range.

418

419 Discrepancies between Goldberg et al. (2021) and our emissions are not as  
 420 straightforward to diagnose, as Goldberg et al. (2021) use NO<sub>2</sub> VCDs from a different sensor  
 421 (OMI) and apply a systematic 37% increase to NO<sub>x</sub> emissions to correct for a low bias in OMI  
 422 attributed to the coarse resolution a priori used in the NO<sub>2</sub> VCDs retrieval. Sampling area  
 423 choice may also be a factor. For example, the smallest of our 54 areas yields NO<sub>x</sub> emissions of  
 424 102 mol s<sup>-1</sup> for Singapore that is 10 mol s<sup>-1</sup> less than the mean of all EMG fits. Goldberg et al.  
 425 (2021) used year-round OMI data for all cities except Delhi and Karachi. As these cities are  
 426 north of 25°N, only May-September observations were used by Goldberg et al. (2021). We find  
 427 that Delhi and Karachi mean May-September TROPOMI NO<sub>2</sub> VCDs in 2019 averaged within  
 428 the 4° × 4° domain selected for each city (Figure 2(a)-(b)) are 11-12% less than those in  
 429 October-April, due to the shorter photochemical lifetime of NO<sub>x</sub> in the warmer months. Open  
 430 biomass burning emissions also influence seasonality in the TROPOMI NO<sub>2</sub> VCDs, but the  
 431 EMG fit accounts for this by distinguishing background NO<sub>2</sub> (*B* in Equation (1)) from NO<sub>2</sub> in  
 432 the city plume (*a* in Equation (1)).

433 We find that if we apply the EMG fit to individual months for Delhi and Karachi, all  
 434 54 EMG fits fail for Delhi in July-August and yield spurious results in September due to large  
 435 data loss resulting from persistent clouds during the monsoon season. All 12 months are  
 436 retained for Karachi, Singapore and Manila. November-April mean values of *a* are 21% more  
 437 than in May-October for Karachi, 9% more for Singapore, and 39% more for Manila. This  
 438 suggests that using NO<sub>2</sub> VCDs for a portion of the year may yield systematic biases in

439 emissions that may not reflect seasonality in the underlying activities affecting the emissions.  
440 Larger wintertime than summertime emissions have also been reported in the global study of  
441 Lange et al. (2022). They quantified summer-to-winter emission ratios of  $\sim 0.5$  for Colombo  
442 and Delhi. The top-down emissions calculation (Equation (3)) does not fully account for  
443 seasonality in photochemistry. The derived effective  $\text{NO}_x$  lifetimes used to calculate  $\text{NO}_x$   
444 emissions (Equation (2)) are mostly influenced by dispersion. As a result, the effective lifetimes  
445 are much shorter than the expected chemical lifetimes of  $\text{NO}_x$  (de Foy et al., 2014). In the  
446 synthetic experiment scenarios tested by de Foy et al. (2014), the EMG fit applied to wind  
447 rotated data yielded an effective lifetime of 4 h for a 12-h chemical lifetime scenario. According  
448 to Shah et al. (2020), the chemical lifetime of  $\text{NO}_x$  for central-eastern China centred at  $\sim 35^\circ\text{N}$ ,  
449 the northerly portion of our domain, ranges from  $\sim 6$  h in summer to  $\sim 24$  h in winter. None of  
450 the monthly effective lifetimes for our target cities reproduces this seasonality and the longest  
451 lifetime is  $13.3 \pm 3.7$  h for Yangon in November. The implication is that the size of absolute  
452 emissions derived with sub-annual satellite data may be biased, but should have negligible  
453 effect if used to quantify relative trends, as in Goldberg et al. (2021) and Laughner & Cohen  
454 (2019), for example.

455

### 456 **3.4 Comparison to Bottom-up Emissions**

457 Figure 5 compares annual top-down and bottom-up  $\text{NO}_x$  emissions. According to our  
458 HEMCO simulations, anthropogenic sources account for most ( $>87\%$ ) annual  $\text{NO}_x$  emissions.  
459 The relative differences between our top-down estimates and the bottom-up inventory are  
460 within 50% for Mumbai (1%), Bangkok (2%), Chennai (9%), Ahmedabad (11%), Kolkata  
461 (21%), Singapore (21%), Bangalore (32%), Manila (35%), and Kuala Lumpur (46%). A 50-  
462 100% difference occurs for Ho Chi Minh City (53%), Jakarta (54%), Delhi (64%), and  
463 Colombo (91%). Even greater relative differences occur for Karachi (2.1 times), Islamabad  
464 (2.1 times), Lahore (2.4 times), Yangon (3.3 times), Dhaka (6.9 times), and Kabul (11-fold).  
465 The largest absolute discrepancies are for Dhaka and Jakarta. Bottom-up emissions are  $107$   
466  $\text{mol s}^{-1}$  less than the top-down values for Dhaka and  $78 \text{ mol s}^{-1}$  more for Jakarta. On a mass  
467 basis, this is equivalent to a  $155 \text{ Gg NO}_x$  as  $\text{NO}_2$  underestimate for Dhaka and a  $113 \text{ Gg NO}_x$   
468 as  $\text{NO}_2$  overestimate for Jakarta.

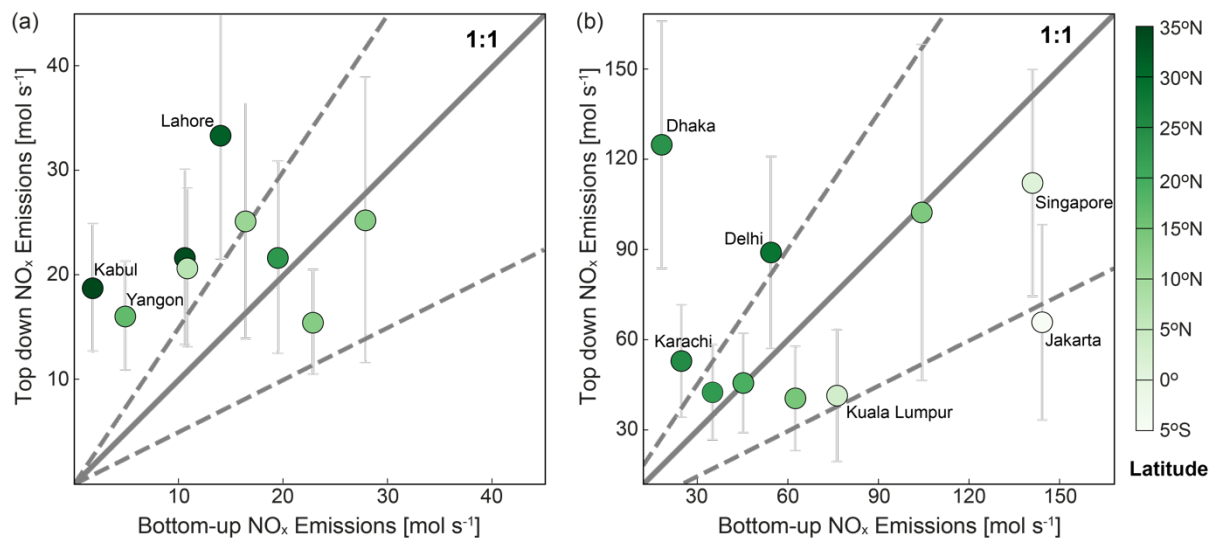
469 The different years used (2018 for HTAP, 2019 for TROPOMI) should at most account  
470 for a 14% difference in emissions, based on the size of annual trends inferred by Vohra et al.  
471 (2022) using long-term observations of OMI  $\text{NO}_2$  VCDs over large and fast-growing cities in  
472 South and Southeast Asia. Vohra et al. (2022) identified that emission inventories do not  
473 capture the steep decline in  $\text{NO}_x$  emissions in Jakarta attributed to national policies targeting  
474 vehicles. In addition to misrepresenting annual changes in underlying activities, the emission  
475 factors are mostly informed by studies in China and Japan (Kurokawa & Ohara, 2020). The  
476 bottom-up and top-down emissions differences for many cities also exceed the  $\pm 30\%$   
477 difference that results from the choice of bottom-up emissions grid sampling and the  $\pm 30\%$   
478 difference from the timing of the top-down (midday) and bottom-up (24-h) estimates inferred  
479 by Goldberg et al. (2021).

480 Apparent in Figure 5 is a latitudinal pattern in the discrepancies. Top-down emissions  
481 are greater than bottom-up emissions for cities to the north and vice versa for cities to the south,  
482 so that in general top-down emissions exceed bottom-up emissions in South Asia and vice  
483 versa in Southeast Asia.  $\text{NO}_x$  chemical loss varies with latitude, due to variability in the amount  
484 of sunlight available to form hydroxyl and peroxy radicals required to form  $\text{HNO}_3$  and organic  
485 nitrates, the main daytime chemical loss pathway for  $\text{NO}_x$ . This latitudinal pattern is likely

486 because the EMG fit also does not fully account for spatial variability in NO<sub>x</sub> photochemistry,  
 487 imparting a bias in the top-down emissions. The size of this bias will depend on the relative  
 488 contribution of NO<sub>x</sub> chemical loss to total loss in the wind rotated plume.

489

490



491

492 **Figure 5.** Comparison of annual top-down and bottom-up NO<sub>x</sub> emissions for target cities. Data  
 493 are coloured by city centre latitude and split into top-down NO<sub>x</sub> emissions < 40 mol s<sup>-1</sup> (a) and  
 494 ≥ 40 mol s<sup>-1</sup> (b). Error bars are the overall uncertainty in top-down emissions estimates. Grey  
 495 lines indicate 1:1 agreement (solid) and ±50% difference (dashed). The bottom-up emissions  
 496 sampling extent of each city is in Figure S1. Data used to generate the figure are in Table S1.

497

#### 498 4 Conclusions

499 City nitrogen oxides (NO<sub>x</sub>) emissions can be derived with a now well-established  
 500 approach using satellite observations of nitrogen dioxide (NO<sub>2</sub>), wind rotation and a Gaussian  
 501 fit to the city plume. Issues with this approach are that the choice of sampling area around the  
 502 city centre is not standardized and so is prone to subjective area selection and the Gaussian fit  
 503 often fails or yields non-physical best-fit parameters. Here we address these issues by applying  
 504 54 sampling areas to isolated cities. We test our method with TROPospheric Monitoring  
 505 Instrument (TROPOMI) NO<sub>2</sub> observations for 2019 over 19 large, isolated cities in South and  
 506 Southeast Asia that lack contemporary, publicly available bottom-up emissions estimates.

507 Annual NO<sub>x</sub> emissions, obtained for all 19 cities, are < 73 Gg NO<sub>x</sub> as NO<sub>2</sub> a<sup>-1</sup> for most  
 508 cities, between 73-145 Gg NO<sub>x</sub> as NO<sub>2</sub> a<sup>-1</sup> for Karachi, Delhi, and Jakarta and > 145 Gg NO<sub>x</sub>  
 509 as NO<sub>2</sub> a<sup>-1</sup> for Bangkok, Dhaka, and Singapore. The overall uncertainty in the annual emissions  
 510 is 30-60%. Our emissions estimates are in general ~27% more than past studies that use a single  
 511 sampling area, due to differences in satellite data products and months targeted. The latter we  
 512 suggest may lead to biases, as the top-down emissions estimate does not properly account for  
 513 seasonality in photochemical loss of NO<sub>x</sub>. Relative differences between our top-down estimates  
 514 and a widely used bottom-up inventory are < 50% for 9 of the 19 cities, within 50-100% for  
 515 Ho Chi Minh City, Jakarta, Delhi, and Colombo, and much greater for Karachi (2.1 times),  
 516 Islamabad (2.1 times), Lahore (2.4 times), Yangon (3.3 times), Dhaka (6.9 times), and Kabul  
 517 (11-fold). There is a latitudinal dependence of the size of these discrepancies that we suggest

518 is because the top-down approach also does not properly account for spatial variability in the  
519 chemical lifetime of NO<sub>x</sub>.

520 The increased success of deriving NO<sub>x</sub> emissions with our updated approach enables  
521 us to identify that further development is needed to account for time and space variability in  
522 the chemical lifetime of NO<sub>x</sub> to fully exploit the top-down approach to interrogate seasonality  
523 in emissions, to validate bottom-up emissions, to exploit hourly observations from  
524 geostationary instruments, and to inform air quality regulation.

## 525 **Data and Software Availability**

526 The TROPOMI tropospheric columns for 2019 are publicly available from the S5P-PAL Data  
527 Portal (<https://data-portal.s5p-pal.com/>). GEOS-Chem source codes are preserved on Zenodo  
528 by The International GEOS-Chem User Community (2021) for GCClassic version 13.3.4 and  
529 by The International GEOS-Chem User Community (2022) for GCHP version 13.4.1.

## 530 **Author Contributions**

531 GL developed the methodology, GL and EAM processed, analysed and interpreted the data.  
532 GL and EAM prepared the manuscript. KV assisted in data collection and analysis. RPH and  
533 DZ conducted the GEOS-Chem simulations (RPH: GCClassic; DZ: GCHP). RVM contributed  
534 to the methodology. SG contributed to interpretation of the results. All co-authors provided  
535 editorial input.

## 536 **Conflicts of interest**

537 The authors declare there are no conflicts of interest.

## 538 **Acknowledgements**

539 This research has been supported by the European Research Council under the European  
540 Union's Horizon 2020 research and innovation programme (through the Starting Grant  
541 awarded to Eloise A. Marais, UpTrop; grant no. 851854). GL is grateful for a PhD studentship  
542 funded by the China Scholarship Council. RVM acknowledges support from NASA Grant  
543 80NSSC21K0508.

## 544 **References**

545 Beirle, S., Boersma, K. F., Platt, U., Lawrence, M. G., & Wagner, T. (2011), Megacity Emissions and  
546 Lifetimes of Nitrogen Oxides Probed from Space, *Science*, 333(6050), 1737-1739,  
547 doi:10.1126/science.1207824.

548 Crippa, M., Guizzardi, D., Butler, T., Keating, T., Wu, R., Kaminski, J., et al. (2023), The HTAP\_v3  
549 emission mosaic: merging regional and global monthly emissions (2000-2018) to support air quality  
550 modelling and policies, *Earth System Science Data*, 15(6), 2667-2694, doi:10.5194/essd-15-2667-2023.

551 Curier, R. L., Kranenburg, R., Segers, A. S., Timmermans, R. M. A., & Schaap, M. (2014), Synergistic  
552 use of OMI NO<sub>2</sub> tropospheric columns and LOTOS-EUROS to evaluate the NO<sub>x</sub> emission trends across  
553 Europe, *Remote Sensing of Environment*, 149, 58-69, doi:10.1016/j.rse.2014.03.032.

554 de Foy, B., Wilkins, J. L., Lu, Z. F., Streets, D. G., & Duncan, B. N. (2014), Model evaluation of  
555 methods for estimating surface emissions and chemical lifetimes from satellite data, *Atmospheric  
556 Environment*, 98, 66-77, doi:10.1016/j.atmosenv.2014.08.051.

- 557 de Foy, B., Lu, Z. F., & Streets, D. G. (2016), Satellite NO<sub>2</sub> retrievals suggest China has exceeded its  
558 NO<sub>x</sub> reduction goals from the twelfth Five-Year Plan, *Scientific Reports*, 6, 9, doi:10.1038/srep35912.
- 559 Eastham, S. D., Long, M. S., Keller, C. A., Lundgren, E., Yantosca, R. M., Zhuang, J., et al. (2018),  
560 GEOS-Chem High Performance (GCHP v11-02c): a next-generation implementation of the GEOS-  
561 Chem chemical transport model for massively parallel applications, *Geoscientific Model Development*,  
562 11(7), 2941-2953, doi:10.5194/gmd-11-2941-2018.
- 563 Eskes, H., van Geffen, J., Sneep, M., Veefkind, P., Niemeijer, S., & Zehner, C. (2021), S5P Nitrogen  
564 Dioxide v02.03.01 intermediate reprocessing on the S5P-PAL system: Readme file.
- 565 Goldberg, D. L., Lu, Z. F., Oda, T., Lamsal, L. N., Liu, F., Griffin, D., et al. (2019a), Exploiting OMI  
566 NO<sub>2</sub> satellite observations to infer fossil-fuel CO<sub>2</sub> emissions from US megacities, *Science of the Total  
567 Environment*, 695, 9, doi:10.1016/j.scitotenv.2019.133805.
- 568 Goldberg, D. L., Lu, Z. F., Streets, D. G., de Foy, B., Griffin, D., McLinden, C. A., et al. (2019b),  
569 Enhanced Capabilities of TROPOMI NO<sub>2</sub>: Estimating NO<sub>x</sub> from North American Cities and Power  
570 Plants, *Environmental Science & Technology*, 53(21), 12594-12601, doi:10.1021/acs.est.9b04488.
- 571 Goldberg, D. L., Anenberg, S. C., Lu, Z. F., Streets, D. G., Lamsal, L. N., McDuffie, E. E., & Smith, S.  
572 J. (2021), Urban NO<sub>x</sub> emissions around the world declined faster than anticipated between 2005 and  
573 2019, *Environmental Research Letters*, 16(11), 11, doi:10.1088/1748-9326/ac2c34.
- 574 Grulke, N. E., & Heath, R. L. (2020), Ozone effects on plants in natural ecosystems, *Plant Biology*, 22,  
575 12-37, doi:10.1111/plb.12971.
- 576 Hoornweg, D., & Pope, K. (2017), Population predictions for the world's largest cities in the 21st  
577 century, *Environment and Urbanization*, 29(1), 195-216, doi:10.1177/0956247816663557.
- 578 Kurokawa, J., & Ohara, T. (2020), Long-term historical trends in air pollutant emissions in Asia:  
579 Regional Emission inventory in ASia (REAS) version 3, *Atmospheric Chemistry and Physics*, 20(21),  
580 12761-12793, doi:10.5194/acp-20-12761-2020.
- 581 Lange, K., Richter, A., & Burrows, J. P. (2022), Variability of nitrogen oxide emission fluxes and  
582 lifetimes estimated from Sentinel-5P TROPOMI observations, *Atmospheric Chemistry and Physics*,  
583 22(4), 2745-2767, doi:10.5194/acp-22-2745-2022.
- 584 Laughner, J. L., & Cohen, R. C. (2019), Direct observation of changing NO<sub>x</sub> lifetime in North American  
585 cities, *Science*, 366(6466), 723-+, doi:10.1126/science.aax6832.
- 586 Lelieveld, J., Evans, J. S., Fnais, M., Giannadaki, D., & Pozzer, A. (2015), The contribution of outdoor  
587 air pollution sources to premature mortality on a global scale, *Nature*, 525(7569), 367-+,  
588 doi:10.1038/nature15371.
- 589 Li, M., Zhang, Q., Kurokawa, J., Woo, J. H., He, K. B., Lu, Z. F., et al. (2017), MIX: a mosaic Asian  
590 anthropogenic emission inventory under the international collaboration framework of the MICS-Asia  
591 and HTAP, *Atmospheric Chemistry and Physics*, 17(2), 935-963, doi:10.5194/acp-17-935-2017.

592 Lin, H. P., Jacob, D. J., Lundgren, E. W., Sulprizio, M. P., Keller, C. A., Fritz, T. M., et al. (2021),  
593 Harmonized Emissions Component (HEMCO) 3.0 as a versatile emissions component for atmospheric  
594 models: application in the GEOS-Chem, NASA GEOS, WRF-GC, CESM2, NOAA GEFS-Aerosol,  
595 and NOAA UFS models, *Geoscientific Model Development*, *14*(9), 5487-5506, doi:10.5194/gmd-14-  
596 5487-2021.

597 Liu, F., Tao, Z. N., Beirle, S., Joiner, J., Yoshida, Y., Smith, S. J., et al. (2022), A new method for  
598 inferring city emissions and lifetimes of nitrogen oxides from high-resolution nitrogen dioxide  
599 observations: a model study, *Atmospheric Chemistry and Physics*, *22*(2), 1333-1349, doi:10.5194/acp-  
600 22-1333-2022.

601 Lorente, A., Boersma, K. F., Eskes, H. J., Veefkind, J. P., van Geffen, J., de Zeeuw, M. B., et al. (2019),  
602 Quantification of nitrogen oxides emissions from build-up of pollution over Paris with TROPOMI,  
603 *Scientific Reports*, *9*, 10, doi:10.1038/s41598-019-56428-5.

604 Lu, Z., Streets, D. G., de Foy, B., Lamsal, L. N., Duncan, B. N., & Xing, J. (2015), Emissions of nitrogen  
605 oxides from US urban areas: estimation from Ozone Monitoring Instrument retrievals for 2005-2014,  
606 *Atmospheric Chemistry and Physics*, *15*(18), 10367-10383, doi:10.5194/acp-15-10367-2015.

607 Luo, L., Wu, Y. F., Xiao, H. Y., Zhang, R. J., Lin, H., Zhang, X. L., & Kao, S. J. (2019), Origins of  
608 aerosol nitrate in Beijing during late winter through spring, *Science of the Total Environment*, *653*, 776-  
609 782, doi:10.1016/j.scitotenv.2018.10.306.

610 Marais, E. A., Kelly, J. M., Vohra, K., Li, Y. F., Lu, G. D., Hina, N., & Rowe, E. C. (2023), Impact of  
611 Legislated and Best Available Emission Control Measures on UK Particulate Matter Pollution,  
612 Premature Mortality, and Nitrogen-Sensitive Habitats, *Geohealth*, *7*(10), doi:10.1029/2023gh000910.

613 Marvin, M. R., Palmer, P. I., Latter, B. G., Siddans, R., Kerridge, B. J., Latif, M. T., & Khan, M. F.  
614 (2021), Photochemical environment over Southeast Asia primed for hazardous ozone levels with influx  
615 of nitrogen oxides from seasonal biomass burning, *Atmospheric Chemistry and Physics*, *21*(3), 1917-  
616 1935, doi:10.5194/acp-21-1917-2021.

617 McDuffie, E. E., Smith, S. J., O'Rourke, P., Tibrewal, K., Venkataraman, C., Marais, E. A., et al. (2020),  
618 A global anthropogenic emission inventory of atmospheric pollutants from sector- and fuel-specific  
619 sources (1970-2017): an application of the Community Emissions Data System (CEDS), *Earth System  
620 Science Data*, *12*(4), 3413-3442, doi:10.5194/essd-12-3413-2020.

621 Miyazaki, K., Eskes, H. J., Sudo, K., & Zhang, C. (2014), Global lightning NO<sub>x</sub> production estimated  
622 by an assimilation of multiple satellite data sets, *Atmospheric Chemistry and Physics*, *14*(7), 3277-3305,  
623 doi:10.5194/acp-14-3277-2014.

624 Murray, L. T., Jacob, D. J., Logan, J. A., Hudman, R. C., & Koshak, W. J. (2012), Optimized regional  
625 and interannual variability of lightning in a global chemical transport model constrained by LIS/OTD  
626 satellite data, *Journal of Geophysical Research-Atmospheres*, *117*, 14, doi:10.1029/2012jd017934.

627 Pope, R. J., Kelly, R., Marais, E. A., Graham, A. M., Wilson, C., Harrison, J. J., et al. (2022), Exploiting  
628 satellite measurements to explore uncertainties in UK bottom-up NO<sub>x</sub> emission estimates, *Atmospheric  
629 Chemistry and Physics*, *22*(7), 4323-4338, doi:10.5194/acp-22-4323-2022.

- 630 Potts, D. A., Marais, E. A., Boesch, H., Pope, R. J., Lee, J., Drysdale, W., et al. (2021), Diagnosing air  
631 quality changes in the UK during the COVID-19 lockdown using TROPOMI and GEOS-Chem,  
632 *Environmental Research Letters*, 16(5), doi:10.1088/1748-9326/abde5d.
- 633 Randerson, J. T., Van Der Werf, G. R., Giglio, L., Collatz, G. J., & Kasibhatla, P. S. (2017), Global  
634 Fire Emissions Database, Version 4.1 (GFEDv4), 10.3334/ORNLDAAC/1293.
- 635 Shah, V., Jacob, D. J., Li, K., Silvern, R. F., Zhai, S., Liu, M., et al. (2020), Effect of changing NO<sub>x</sub>  
636 lifetime on the seasonality and long-term trends of satellite-observed tropospheric NO<sub>2</sub> columns over  
637 China, *Atmospheric Chemistry and Physics*, 20(3), 1483-1495, doi:10.5194/acp-20-1483-2020.
- 638 Sillman, S. (1999), The relation between ozone, NO<sub>x</sub> and hydrocarbons in urban and polluted rural  
639 environments, *Atmospheric Environment*, 33(12), 1821-1845, doi:10.1016/s1352-2310(98)00345-8.
- 640 Silvern, R. F., Jacob, D. J., Mickley, L. J., Sulprizio, M. P., Travis, K. R., Marais, E. A., et al. (2019),  
641 Using satellite observations of tropospheric NO<sub>2</sub> columns to infer long-term trends in US NO<sub>x</sub> emissions:  
642 the importance of accounting for the free tropospheric NO<sub>2</sub> background, *Atmospheric Chemistry and  
643 Physics*, 19(13), 8863-8878, doi:10.5194/acp-19-8863-2019.
- 644 Sun, K., Zhu, L., Cady-Pereira, K., Miller, C. C., Chance, K., Clarisse, L., et al. (2018), A physics-  
645 based approach to oversample multi-satellite, multispecies observations to a common grid, *Atmospheric  
646 Measurement Techniques*, 11(12), 6679-6701, doi:10.5194/amt-11-6679-2018.
- 647 The International GEOS-Chem User Community (2021). *GCClassic version 13.3.4. Zenodo [software]*.  
648 doi:<https://doi.org/10.5281/zenodo.5764874>.
- 649 The International GEOS-Chem User Community (2022). *GCHP version 13.4.1. Zenodo [software]*.  
650 doi:<https://doi.org/10.5281/zenodo.6564711>.
- 651 Tzortziou, M., Kwong, C. F., Goldberg, D., Schiferl, L., Commane, R., Abuhassan, N., et al. (2022),  
652 Declines and peaks in NO<sub>2</sub> pollution during the multiple waves of the COVID-19 pandemic in the New  
653 York metropolitan area, *Atmospheric Chemistry and Physics*, 22(4), 2399-2417, doi:10.5194/acp-22-  
654 2399-2022.
- 655 Valin, L. C., Russell, A. R., & Cohen, R. C. (2013), Variations of OH radical in an urban plume inferred  
656 from NO<sub>2</sub> column measurements, *Geophysical Research Letters*, 40(9), 1856-1860,  
657 doi:10.1002/grl.50267.
- 658 van Geffen, J., Boersma, K. F., Eskes, H., Sneep, M., ter Linden, M., Zara, M., & Veefkind, J. P. (2020),  
659 S5P TROPOMI NO<sub>2</sub> slant column retrieval: method, stability, uncertainties and comparisons with OMI,  
660 *Atmospheric Measurement Techniques*, 13(3), 1315-1335, doi:10.5194/amt-13-1315-2020.
- 661 van Geffen, J., Eskes, H., Boersma, K. F., & Veefkind, P. (2021), TROPOMI ATBD of the total and  
662 tropospheric NO<sub>2</sub> data products (issue 2.2.0), Royal Netherlands Meteorological Institute (KNMI), De  
663 Bilt, the Netherlands.
- 664 van Geffen, J., Eskes, H., Compernelle, S., Pinardi, G., Verhoelst, T., Lambert, J.-C., et al. (2022),  
665 Sentinel-5P TROPOMI NO<sub>2</sub> retrieval: impact of version v2.2 improvements and comparisons with OMI  
666 and ground-based data, *Atmospheric Measurement Techniques*, 15(7), 2037-2060, doi:10.5194/amt-15-  
667 2037-2022.

- 668 Verstraeten, W. W., Boersma, K. F., Douros, J., Williams, J. E., Eskes, H., Liu, F., et al. (2018), Top-  
669 Down NO<sub>x</sub> Emissions of European Cities Based on the Downwind Plume of Modelled and Space-Borne  
670 Tropospheric NO<sub>2</sub> Columns, *Sensors*, 18(9), doi:10.3390/s18092893.
- 671 Vohra, K., Marais, E. A., Suckra, S., Kramer, L., Bloss, W. J., Sahu, R., et al. (2021), Long-term trends  
672 in air quality in major cities in the UK and India: a view from space, *Atmospheric Chemistry and Physics*,  
673 21(8), 6275-6296, doi:10.5194/acp-21-6275-2021.
- 674 Vohra, K., Marais, E. A., Bloss, W. J., Schwartz, J., Mickley, L. J., Van Damme, M., et al. (2022),  
675 Rapid rise in premature mortality due to anthropogenic air pollution in fast-growing tropical cities from  
676 2005 to 2018, *Science Advances*, 8(14), 13, doi:10.1126/sciadv.abm4435.
- 677 Weng, H. J., Lin, J. T., Martin, R., Millet, D. B., Jaeglé, L., Ridley, D., et al. (2020), Global high-  
678 resolution emissions of soil NO<sub>x</sub>, sea salt aerosols, and biogenic volatile organic compounds, *Scientific*  
679 *Data*, 7(1), 15, doi:10.1038/s41597-020-0488-5.
- 680 Wu, N., Geng, G. N., Yan, L., Bi, J. Z., Li, Y. S., Tong, D., et al. (2021), Improved spatial representation  
681 of a highly resolved emission inventory in China: evidence from TROPOMI measurements,  
682 *Environmental Research Letters*, 16(8), 11, doi:10.1088/1748-9326/ac175f.
- 683 Yue, X., Unger, N., Harper, K., Xia, X. G., Liao, H., Zhu, T., et al. (2017), Ozone and haze pollution  
684 weakens net primary productivity in China, *Atmospheric Chemistry and Physics*, 17(9), 6073-6089,  
685 doi:10.5194/acp-17-6073-2017.
- 686 Zhang, L., Jacob, D. J., Knipping, E. M., Kumar, N., Munger, J. W., Carouge, C. C., et al. (2012),  
687 Nitrogen deposition to the United States: distribution, sources, and processes, *Atmospheric Chemistry*  
688 *and Physics*, 12(10), 4539-4554, doi:10.5194/acp-12-4539-2012.
- 689